Journal of Magnetic Resonance 214 (2012) 51–60

Contents lists available at SciVerse ScienceDirect

Journal of Magnetic Resonance

journal homepage: www.elsevier.com/locate/jmr

Estimation of pore size in a microstructure phantom using the optimised gradient waveform diffusion weighted NMR sequence

Bernard Siow [a,b,*], Ivana Drobnjak [a], Aritrick Chatterjee [c], Mark F. Lythgoe [b], Daniel C. Alexander [a]

[a] Centre for Medical Image Computing, Department of Computer Science, University College London (UCL), Gower Street, London WC1E 6BT, UK
[b] Centre for Advanced Biomedical Imaging (CABI), Department of Medicine and Institute of Child Health, University College London (UCL), London WC1E 6DD, UK
[c] Department of Medical Physics and Bioengineering, University College London (UCL), Gower Street, London WC1E 6BT, UK

ARTICLE INFO

Article history:
Received 9 May 2011
Revised 21 September 2011
Available online 13 October 2011

Keywords:
Axon diameter
Microstructure imaging
Generalised gradient waveform
Diffusion MR
Oscillating gradients
Pore size
Microcapillary fibres
PGSE
OGSE
ActiveAx

ABSTRACT

There has been increasing interest in nuclear magnetic resonance (NMR) techniques that are sensitive to diffusion of molecules containing NMR visible nuclei for the estimation of microstructure parameters. A microstructure parameter of particular interest is pore radius distribution. A recent in silico study optimised the shape of the gradient waveform in diffusion weighted spin-echo experiments for estimating pore size. The study demonstrated that optimised gradient waveform (GEN) protocols improve pore radius estimates compared to optimised pulse gradient spin-echo (PGSE) protocols, particularly at shorter length scales. This study assesses the feasibility of implementing GEN protocols on a small bore 9.4 T scanner and verifies their additional sensitivity to pore radius. We implement GEN and PGSE protocols optimised for pore radii of 1, 2.5, 5, 7.5, 10 μm and constrained to maximum gradient strengths of 40, 80, 200 mT m^{-1}. We construct microstructure phantoms, which have a single pore radius for each phantom, using microcapillary fibres. The measured signal shows good agreement with simulated signal, strongly indicating that the GEN waveforms can be implemented on a 9.4 T system. We also demonstrate that GEN protocols provide improved sensitivity to the smaller pore radii when compared to optimised PGSE protocols, particularly at the lower gradient amplitudes investigated in this study. Our results suggest that this improved sensitivity of GEN protocols would be reflected in clinical scenarios.

1. Introduction

The magnitude of the signal from diffusion weighted (DW) magnetic resonance (MR) techniques is attenuated by the incoherent displacement of molecules containing the nuclei being studied at typical time scales of units to tens of milliseconds. In the case of diffusing molecules in fluids in porous materials, the dispersion pattern of the molecules in the fluid is influenced by the size and shape of the pores. Thus, DW-MR techniques are sensitive to the microstructure of porous materials [1] and have been used in diverse applications for the drilling industry [2], the food industry [3–6], studying minerals [7] and biomedical sciences [8–10].

For our study, we are primarily motivated by biomedical applications and, in particular, the mapping of axon radius in white matter regions of the central nervous system. Axon radii in human white matter tissue range from 0.1 to 10 μm [11]. Axon radius is related to the conduction velocity in myelinated nerve fibres [12]: axon bundles with large axon radii are able to transmit information more quickly, whereas axon bundles with small axon radii can be packed more densely and thus transmit more information per unit cross sectional area. For example, in the corpus callosum, the mode of the axon radius distribution is greater in the midbody, which interconnects sensory areas, than in genu, which interconnects prefrontal areas [11]. As well as providing insight into the structure and function of normal tissue, estimating axon radius distributions may provide useful progression and classification biomarkers for abnormal pathologies such as autism [13], amyotrophic lateral sclerosis (ALS) [14,15] or schizophrenia [16].

The apparent diffusion coefficient (ADC) and the diffusion tensor (DT) are measures of diffusion that assume Gaussian dispersion patterns of diffusing molecules. Studies have used ADC and DT to elucidate microstructural information, such as fibre tract organisation in white matter [8,17]. However, these studies do not attempt to quantify specific properties of the underlying microstructure, such as cell size and density, directly. Estimating the underlying microstructure parameters can be achieved by fitting tissue models to the measured signal, thus improving specificity compared to ADC and DT. For example, in a previous study investigating bovine optic nerve [18], a three compartment model of white matter tissue (ellipsoidal axons, spherical glial cells and extracellular space) is used to estimate nine microstructure

* Corresponding author at: Centre for Medical Image Computing, Department of Computer Science, University College London (UCL), Gower Street, London WC1E 6BT, UK. Fax: +44 20 7387 1397.
E-mail address: b.siow@cs.ucl.ac.uk (B. Siow).

1090-7807/$ - see front matter © 2011 Elsevier Inc. All rights reserved.
doi:10.1016/j.jmr.2011.10.004

parameters (pore dimensions, interface permeability, diffusivity, and volume fraction of the compartments). The composite hindered and restricted model of diffusion (CHARMED) [19,20] is a simpler, two compartment model consisting of parallel axons with a gamma distribution of radii in free extracellular space. A further simplification, the ActiveAx technique [21,22] (single axon radius rather than a distribution) is used to test the feasibility of recovering parameter estimates in experiments in which there is no prior knowledge of fibre orientation. In addition to reducing the model to the smallest realistic set of parameters, another key step for achieving orientational invariant parameter estimates is to optimise the protocol.

Hitherto, trapezoid magnetic field gradients are most commonly used to sensitise the MR signal to diffusion. This technique is used in all the studies mentioned above, [18,21,22], as well as [23–25] to quantify axon radii directly. Pore radius in white matter phantoms has also been quantified, for example in [26–28], using q-space techniques [29,30] and in [31–33] using double wave-vector techniques [34]. Studies that use experiment design optimisation [21,22,35] suggest a single pair of trapezoid gradients requires large gradient amplitudes, which are not currently achievable in most clinical systems, to distinguish small axon radii. Replacing the trapezoid gradients with oscillating waveforms potentially increases sensitivity at short length scales [35–40]. In this text, we use the term PGSE to refer to spin-echo experiments with a pair of diffusion sensitising gradients that each have the same single trapezoid waveform. A recent in silico study optimises iteratively the shape of the gradient waveforms to maximise sensitivity to various pore radii [35]. The optimised 'GEN' waveforms in that study predominantly have the form of oscillating trapezoids, but also include waveforms with slow ramps and less regular features. That study found that protocols that use GEN are better able to distinguish between small axon radii compared to optimised PGSE protocols.

The motivation for this study is twofold: First, we aim to determine whether GEN protocols, which contain diverse waveforms, can be implemented on a small bore scanner. The field experienced by the sample may be perturbed from the intended gradient waveform due to factors such as eddy currents, gradient non-linearities, gradient heating. Indeed, in sequences that have gradients with long duration and/or are switched rapidly (e.g. echo-planar imaging) many of the image artefacts are due to these factors. Second, we compare experimentally the sensitivity of GEN and PGSE protocols to small pore radii (<5 μm) because the majority of axons in human white matter have radii in this range [41].

2. Methods

In Section 2.1, the microcapillary phantoms based on those used in [26] are described. Section 2.2 describes the simplified tissue model based on that used in [21,22,35], and the experiment design optimisation [21] that optimises GEN waveforms and PGSE protocols, as in [35]. Section 2.3 describes the implementation of the GEN and PGSE protocols on a small bore scanner. In Section 2.4, we describe the estimation of microstructural parameters by model fitting to the measured signal. Section 2.5 describes the scanning electron microscopy (SEM) protocol used to measure the distribution of the internal diameters of the fibres.

2.1. Microcapillary phantoms

The microstructure phantoms consist of silica microcapillary fibres with nominal pore radius of 1 ± 0.5, 2.5 ± 1, 5 ± 1, 7.5 ± 1, 10 ± 1 μm (mean ± standard deviation) and outer radius of 75 ± 3 μm (Polymicro Technologies, LLC). For convenience, we use the nominal radius values in the text of this article, unless otherwise stated.

The fibres were provided in 100 m spools, cut to 4 cm lengths, and were soaked in water for a minimum of two weeks. The outer surfaces were then dried, the fibres were packed in 10 mm NMR tubes, and the NMR tubes were filled with Fomblin Perflourosolv™ PFS-1 (a mixture of perfluoropolyethers with a distribution of polymer lengths, Solvay Solexis, Inc.). The Fomblin is meant to provide a proton NMR invisible medium outside the microcapillaries. The intra- to extra-capillary volume ratio is very small ($\approx 1.8 \times 10^{-3}$ for 1 μm microcapillaries), due to large outer radius of the microcapillaries. If water is used instead of Fomblin, then the signal from intra-capillary water would be swamped by that of the extra-capillary water. However, the Fomblin Perflourosolv™ PFS-1 has $-OCF_2H$ as a terminal group (personal communication, Andrea Sergio, Solvay Solexis, Inc., 2010). This results in several peaks approximately 700 Hz offset from the water peak in the NMR spectrum at 9.4 T, thus we only considered the water peak to evaluate the intra-capillary signal.

The Fomblin, as opposed to air, when used as an extra-capillary medium, also serves to reduce unwanted magnetic field gradients due to the reduced difference in susceptibility between the extra-capillary medium and the capillary walls. Susceptibility effects were further reduced by orientating the sample such that the fibres were aligned parallel to the main field and by making the length of the microcapillaries much longer than the sensitive length of the r.f. coil.

2.2. Optimisation

In the following text we use the terms 'protocols', 'repetitions' and 'measurements'. The relationship between them is as follows: A protocol is a set of combinations of pulse sequence parameters. A combination of pulse sequence parameters produces a measurement. For example, for PGSE, each measurement comes from a particular gradient amplitude, δ, and Δ; for GEN each measurement comes from one gradient waveform (the same waveform is played out forwards before the refocusing pulse and backward after). Repetitions are multiple independent acquisitions of one measurement.

The signal model is as described in [21,35] but with the intra-pore volume fraction set to 1, i.e. no extra-pore signal. Briefly, the model assumes the signal comes from water at 18 °C, where the diffusivity is 1.93×10^{-9} m^2 s^{-1} [42], inside parallel cylinders of a single radius with impermeable walls.

We obtained PGSE protocols using the algorithm in [21] adapted for the simplified tissue model described. Briefly, the optimisation searched for the four combinations of $|G|$, δ and Δ (amplitude, duration, and separation of onset of the two gradient pulses) that minimised the sum of Cramer-Rao lower bounds, which is the lower bound on the variance of the estimators of the parameters, on the two parameters of the model, radius and diffusivity. For GEN protocols, the gradient waveform optimisation and the signal model were as in [35]. Each protocol contains just four measurements each with gradient direction fixed perpendicular to the fibre direction, as in [35].

To assess the optimal echo time (TE) for the GEN protocol, trial optimisations for TE = 60, 80, 100, 127 ms for G_{max} = 40 and 200 mT m^{-1} were performed. A maximum TE of 127 ms was chosen because preliminary spin-echo experiments on various phantoms, including agarose only phantoms, showed signal instabilities due to coherent vibrational motion for TE $\gg$ 127 ms. We have not observe this artefact at TE $\leqslant$ 127 ms. The objective function of the optimisation was minimal at the highest TE, and thus TE was set to 127 ms. The rate of change of gradient amplitude was constrained to a maximum of 2500, 1000, 500 T m^{-1} s^{-1}

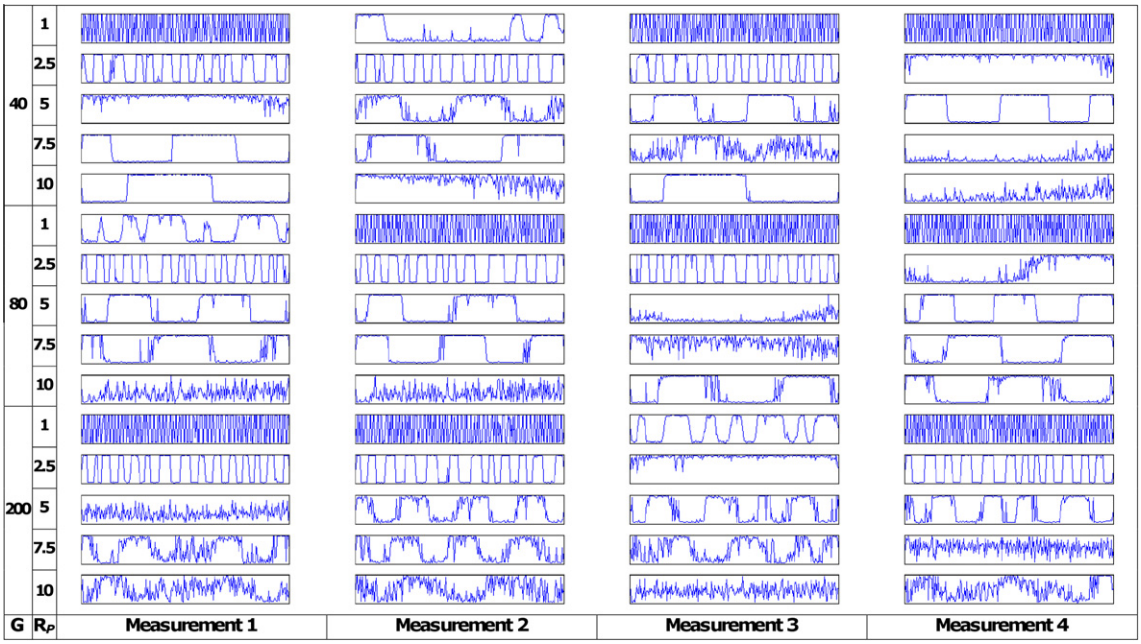

Fig. 1. Optimised gradient waveforms for all GEN protocol. Waveforms are normalised to the gradient amplitude of each set of measurements and all have duration of 50.40 ms. G = Gradient amplitude (mT m^{-1}), R_p = Radius for which protocol was optimised (μm).

Table 1
b-values for GEN and PGSE protocols.

Gradient amplitude/mT m^{-1}	Radius/μm	b-value/sm^{-2}							
		GEN				PGSE			
		M1	M2	M3	M4	M1	M2	M3	M4
40	1	4.63E + 08	1.72E + 07	4.89E + 06	1.80E + 06	3.81E + 08	4.37E + 06	2.66E + 06	1.83E + 06
	2.5	2.18E + 07	2.04E + 07	9.49E + 09	2.00E + 07	2.95E + 09	1.26E + 08	1.38E + 08	7.96E + 07
	5	3.86E + 08	2.19E + 08	8.57E + 09	9.66E + 07	4.11E + 08	4.11E + 08	4.11E + 08	1.74E + 10
	7.5	3.45E + 08	5.02E + 08	1.45E + 08	8.68E + 09	5.95E + 08	5.95E + 08	1.64E + 10	5.95E + 08
	10	4.52E + 08	2.29E + 08	4.20E + 08	5.79E + 09	6.57E + 08	6.57E + 08	8.26E + 09	6.57E + 08
80	1	1.93E + 07	2.43E + 09	2.81E + 07	1.33E + 07	1.02E + 07	2.01E + 07	1.52E + 09	1.16E + 07
	2.5	2.04E + 07	3.06E + 07	1.09E + 09	4.18E + 07	4.35E + 08	1.37E + 08	1.17E + 10	8.81E + 07
	5	5.05E + 08	2.99E + 10	3.93E + 08	4.19E + 08	2.77E + 10	6.95E + 08	6.95E + 08	6.95E + 08
	7.5	7.81E + 08	6.18E + 08	7.54E + 08	1.37E + 10	7.52E + 08	7.52E + 08	1.27E + 10	7.52E + 08
	10	6.60E + 08	6.19E + 09	6.90E + 08	6.95E + 08	7.66E + 08	7.66E + 08	6.49E + 09	7.66E + 08
200	1	1.57E + 08	5.30E + 09	5.63E + 07	5.11E + 07	9.50E + 09	4.31E + 07	6.41E + 07	9.17E + 07
	2.5	1.45E + 08	1.63E + 08	4.65E + 08	1.01E + 11	4.90E + 08	4.91E + 08	6.75E + 10	4.91E + 08
	5	3.43E + 10	7.09E + 08	7.16E + 08	7.80E + 08	9.48E + 08	1.99E + 10	9.48E + 08	9.48E + 08
	7.5	6.86E + 08	1.34E + 10	6.80E + 08	6.69E + 08	9.41E + 09	9.05E + 08	9.05E + 08	9.05E + 08
	10	6.76E + 08	6.35E + 08	6.32E + 08	6.29E + 09	4.89E + 09	8.10E + 08	8.10E + 08	8.10E + 08

for maximum gradient amplitudes of 200, 80, 40 mT m^{-1}, respectively. Each optimised gradient had a duration of 50.4 ms and the separation between the onset of the gradients was 55 ms

We ran the optimisation for both GEN and PGSE protocols 15 times: one for each combination of radius (1, 2.5, 5, 7.5 and 10 μm) and maximum gradient amplitude (40, 80, 200 mT m^{-1}) each with four unique waveforms for a total of 60 waveforms (all shown in Fig. 1). The waveforms are similar to those shown in [35]. The b-values for the GEN and PGSE protocols are found in Table 1.

2.3. Implementation of protocols

A GEN spin echo sequence, reflecting the sequence used in the optimisation, was implemented on a 21 cm bore 9.4 T Varian 400-MR small bore system (Varian, Inc.) running VnmrJ 2.3A software, and equipped with 6 cm bore gradient inserts capable of 1 T m^{-1} with a rise time of 200 μs. A 26 mm diameter birdcage r.f. coil (Rapid Biomedical, GmBH) was used.

Preliminary investigations indicated that residue on the r.f. coil former can contaminate the signal. In order to remove this contamination signal, the 90° excitation and 180° refocusing pulses were made to be slice selective and could be positioned independently. This allowed the slices to be positioned orthogonally to each other, thus only spins in the intersecting cuboid contributed to the spin-echo signal. The position of the intersecting cuboid was set to excite only the sample.

Sequence parameters were as follows: TR = 3 s, TE = 127 ms, 10 mm slices, two averages, receiver bandwidth 4000 Hz, spectral resolution = 62.5 Hz, transmit and receive frequencies were set to the water resonance frequency, 0.8 ms duration refocusing pulse with 80 mT m^{-1} amplitude and 0.5 ms duration slice crushers ('butterfly gradients') orthogonal to the axis of the capillaries. The GEN gradient waveforms in the pulse sequence were identical

to those generated by the optimisation. The same sequence was used for PGSE protocols except that trapezoid waveforms were used and the TE value used was generated by the optimisation.

In order to determine the diffusivity of the intra-capillary water, D_0, we measured the diffusivity parallel to the axis of the fibres using the same PGSE sequence with the following parameters: Δ = 5.5 ms, δ = 3 ms, G = 0, 200, 300, 400, 500, 600 mT m^{-1}, TE = 30 ms. T_2 measurements were made with a Carr–Purcell–Meiboom–Gill sequence with the following parameters: TE = 0.1875, 0.375, 0.75, 1.5, 3, 6 s, interpulse delay = 2 ms, receiver bandwidth = 10000 Hz, spectral resolution = 1.25 Hz, TR = 10 s. High resolution spectra were collected using the pulse-and-collect sequence with the following parameters: receiver bandwidth = 2003 Hz spectral, spectral resolution = 0.125 Hz, 48 averages.

For spatial localisation, we performed multiple average gradient echo imaging scans, each with a duration of ~20 min. These images were used to ensure that the axes of the fibres were parallel to the main field, and to ensure that the diffusion and slice selection gradient were orthogonal to the axis of the fibres. Fortuitously, it was signal from the Fomblin that provided sufficient signal for these scans, particularly for the phantoms with the smallest pores. Shimming and pulse calibration were performed manually using pulse-and-collect sequences.

2.4. Data acquisition

For the GEN protocols, we scanned each phantom with each protocol (four measurements per protocol, for each combination of the 15 GEN protocols and the five phantoms, totalling 300 measurements), repeating each measurement 64 times. For convenience we use 'R_P' to represent the radius for which the protocol is optimised, and 'R_R' to represent the radius of the pores in the phantoms. For the PGSE protocols, we scanned each phantom with the corresponding protocol ($R_P = R_R$) only, repeating each measurement 64 times. The scans were performed in one scan session per phantom, and identical unweighted measurements were taken at the beginning and the end of each scan session. The durations of the GEN and PGSE protocols were 6.4 h and 1.28 h, respectively.

The temperature of the sample was measured throughout the experiments using a MR compatible temperature probe with stated accuracy of ±0.1 °C (Small Animal Instruments, Inc.) in thermal contact with the sample. The temperature was stable at 18.0 ± 0.5 °C.

We find that the repetition with the lowest SNR is greater than 80, for the entire data set for both GEN and PGSE protocols, apart from three measurements: GEN protocol, G = 200 mT m^{-1}, R_P = 2, R_R = 5, 7.5, 10 μm. These measurements are very heavily diffusion weighted and the signals are completely attenuated. In addition, the spectra of the unweighted scans have high SNR (Fig. 2). The high values of SNR are a strong indication that the potential effects of noise bias are small, and should not affect comparisons between GEN and PGSE protocols. We also note that there is clear separation between the peaks due to water and Fomblin indicating that the water signal is not contaminated by the Fomblin signal.

2.5. Simulation and fitting

For each of the 60 waveforms and each of the five fibre radii, we synthesized an expected signal using the modified matrix method for gradients in three dimensions [43], which accounted for the slice selection gradients that added significant diffusion weighting.

Similarly, the fitting of the signal used the Markov Chain Monte Carlo (MCMC) procedure detailed in [21] and the 3D matrix method signal model [43]. Only two model parameters were fitted: the pore radius and the unweighted signal, i.e. the signal without any diffusion weighting (no diffusion or slice selection gradients). For R_R = 1 μm, intra-pore diffusivity was set to the measured D_0 value, 1.70×10^{-9} m^2 s^{-1}. For all other R_R, the reference value of 1.93×10^{-9} m^2 s^{-1} [42] was used because the measured D_0, found in Table 2, fell within 5% of the reference value. To ensure steady-state conditions, we considered only the last 62 of the 64 repetitions. The measured signal from NMR was taken to be the magnitude of the central (water) peak of the Fourier transform of the spin-echo signal. The MCMC procedure in [21] uses a Rician additive noise model, however we find a significant multiplicative noise component in our signal. In fact, we replace the additive noise model with the standard deviation of the signal over the 62 repetitions for each measurement. The unweighted signal was initialised to the measured signal with slice selection gradients but without diffusion gradients. The pore radius was initialised to the nominal radius. Other parameters for the MCMC procedure

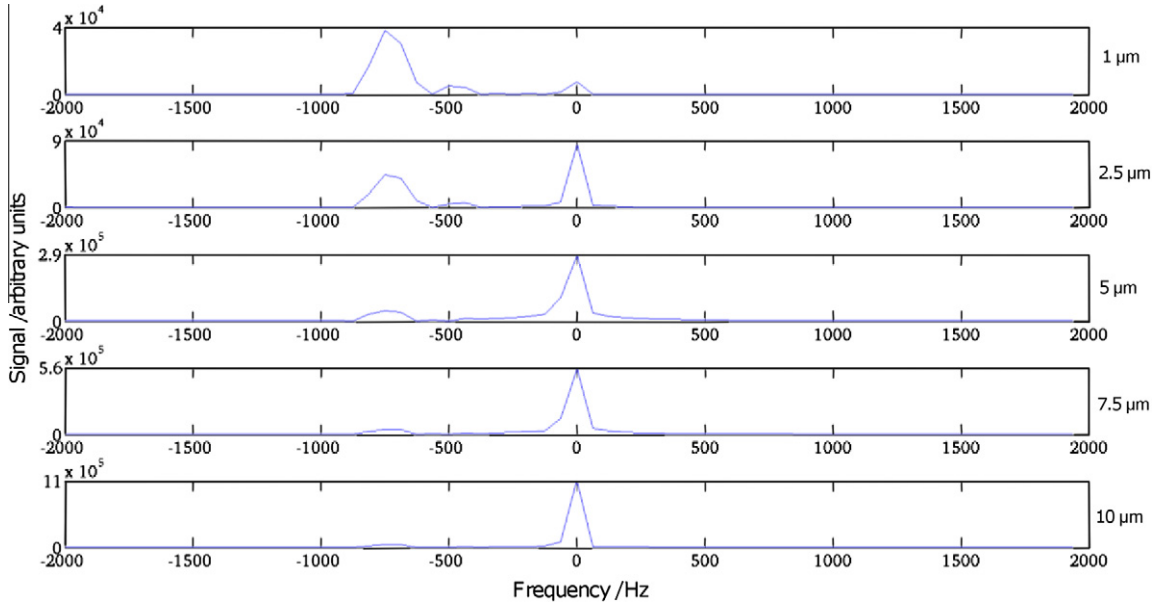

Fig. 2. Spectra with no diffusion weighting for phantoms of the various radii. The water peak is found at 0 Hz and signal from PFS-1 at ~−700 Hz.

Table 2
Properties of the phantoms measured by SEM and MR: α_r – axon radius index, s.d. – standard deviation of the radius measured by SEM, linewidth – full width at half maximum of water peak in high resolution baseline corrected spectra. D_0 – diffusivity parallel to the axis of the fibres, and T_2.

R_R/μm	SEM		MR		
	α_r/μm	s.d./μm	Linewidth/Hz	$D_0/10^{-9}$ m^2 s^{-1}	T_2/ms
1	0.951	0.165	6.28	1.70	662
2.5	2.79	0.331	5.74	1.95	1050
5	5.47	0.455	5.75	1.92	1442
7.5	6.92	0.370	3.70	1.99	1311
10	9.98	0.750	5.75	1.97	1383

were as follows: sample run length of 10^5, burn in of 10^4. Every thousandth sample from the MCMC fitting procedure was taken to construct a histogram representing the posterior distribution on the radius.

2.6. Scanning electron microscopy

SEM was used to measure the inner diameter of the microcapillary fibres. A random sample of 50 fibres was taken from each phantom and dried thoroughly. The fibres were then securely packed in a plastic cylinder with inner diameter of 5 mm and cut to a length of 5 mm. The sample was then evenly 'splutter' coated with a thin layer (of order units of nm) of gold. JEOL Datum JSM-7401F Field Emission Scanning Electron Microscope (JEOL Ltd.) was used to scan the sample. The scan was performed at 9.63×10^{-4} Pa with the following parameters: 2 kV voltage, 9.5 μA current, magnification of 100–7500×. For each fibre, the sample was rotated to ensure the axis of the fibre was normal to the imaging plane. Two diameter measurements were taken per fibre and the average was taken. We then calculate axon diameter index, α, as defined in [22]. We use α instead of mean diameter because the NMR signal from cylinders scales with cross sectional area rather than diameter. For convenience, we divide α by two and use the term axon radius index, α_r.

3. Results

3.1. Scanning electron microscopy

α_r was found to be 0.9507, 2.7940, 5.4694, 6.9208, 9.9831 μm for fibres that have nominal radii, R_R, of 1, 2.5, 5, 7.5, 10 μm, respectively. α_r broadly agrees with the nominal radii, except for $R_R = 5$ and 7.5 μm. Histograms of the distribution of the fibre radii are found in Fig. 3.

3.2. Comparison of measured signal with simulated signal

This experiment assesses whether GEN protocols can be implemented in practice on a small bore MR scanner. We achieve this by comparing the measured signal with simulated signal for GEN protocols. Fig. 4 contains scatter plots of normalised simulated signal against normalised measured signal for each GEN protocol, R_P. Fig. 5 contains the ratio of the measured signal to the simulated signal. For Figs. 4 and 5, α_r values are used for the tissue model to simulate the signal.

Fig. 4 shows that there is a good agreement between the measured and the simulated signal over the vast majority of measurements. Little attenuation occurs for $R_R = 1$ μm, i.e. '+' markers are all clustered near the point (1,1). However, the signals from measurements for $R_R \geqslant 2.5$ μm are more spread out. For $R_R = 5$, 7.5 and 10 μm (circle, square and diamond markers), measurements are spread over the whole range from 0 to 1. Also protocols with

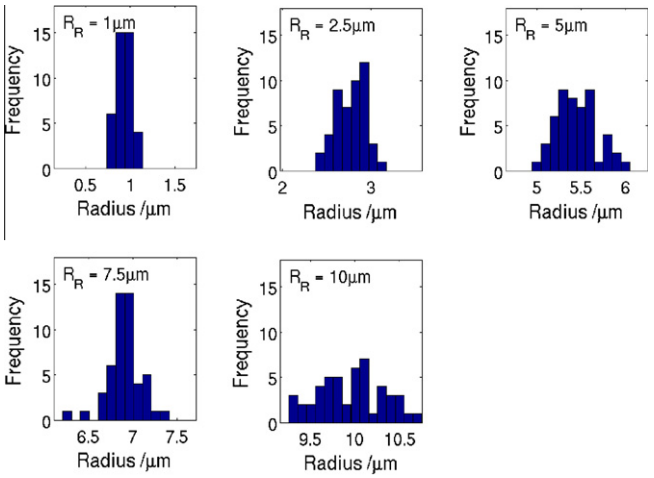

Fig. 3. Histograms of radii as measured by SEM for the various phantoms used in this study.

greater maximum gradient amplitude tend of have measurements with greater attenuation (blue[1] markers tend to be closer to the origin, red markers tend to be closer to 1,1, with green markers in between).

Fig. 5 is the ratio of normalised simulated signal to normalised mean measured signal, for all combinations of R_R and R_P. One observation we can see from Fig. 5 is the drift in the signal within each acquisition set, corresponding to a particular R_R. The order of scans for an acquisition set is (from fastest to slowest loop): measurements, M; then gradient amplitudes, G; then protocol, R_P. This corresponds to going across (left to right), then down the rows in Fig. 5. We see only minor drifts in signal except for: $R_R = 5$ μm, $R_P = 1$ μm, $G = 40$ mT m^{-1} from M1 to M4; and a slow drift across the entire acquisition set for $R_R = 10$ μm.

3.3. Posterior distributions on pore radius

In these experiments, we assess the precision and accuracy of pore radius estimates for GEN and PGSE protocols. We are primarily interested in whether GEN protocols are more sensitive to small pore radii than PGSE protocols. We achieve this by comparing the histograms of the posterior distributions on the pore radius for $R_P = R_R$, i.e. the protocols that are most sensitive to the pore radius in each particular phantom. We then assess the robustness of the GEN protocols. Figs. 6 and 7 show histograms of the posterior distributions on the pore radius for each combination of R_P and R_R. Table 3 shows the mean and standard deviation of the samples from the posterior distribution on the radius, and is grouped by R_P.

Fig. 6 compares the posterior distributions on pore radius for the GEN and PGSE protocols for maximum gradient amplitudes of 40, 80 and 200 mT m^{-1}, for combinations with $R_P = R_R$ only. The mean and standard deviation (SD) of the $R_P = R_R$ distributions are given in the bold rows of Table 3. This combination should show the best case scenario for each particular R_R, i.e. each phantom is scanned with the protocol optimised for radius equal to the nominal radius of the pores in the phantom. By visual inspection of Fig. 6, we see that the posterior distributions are narrower for GEN than for PGSE protocols, particularly for $R_R = 1$ and 2.5 μm at 40 mT m^{-1}. This is reflected in the SD values in Table 3, for example, for $R_R = 2.5$ μm, SD falls from 0.619 μm to 0.169 μm for PGSE and GEN, respectively. For other radii and gradient amplitudes, the standard deviations of the posterior distributions of

[1] For interpretation of color in Figs. 1–7, the reader is referred to the web version of this article.

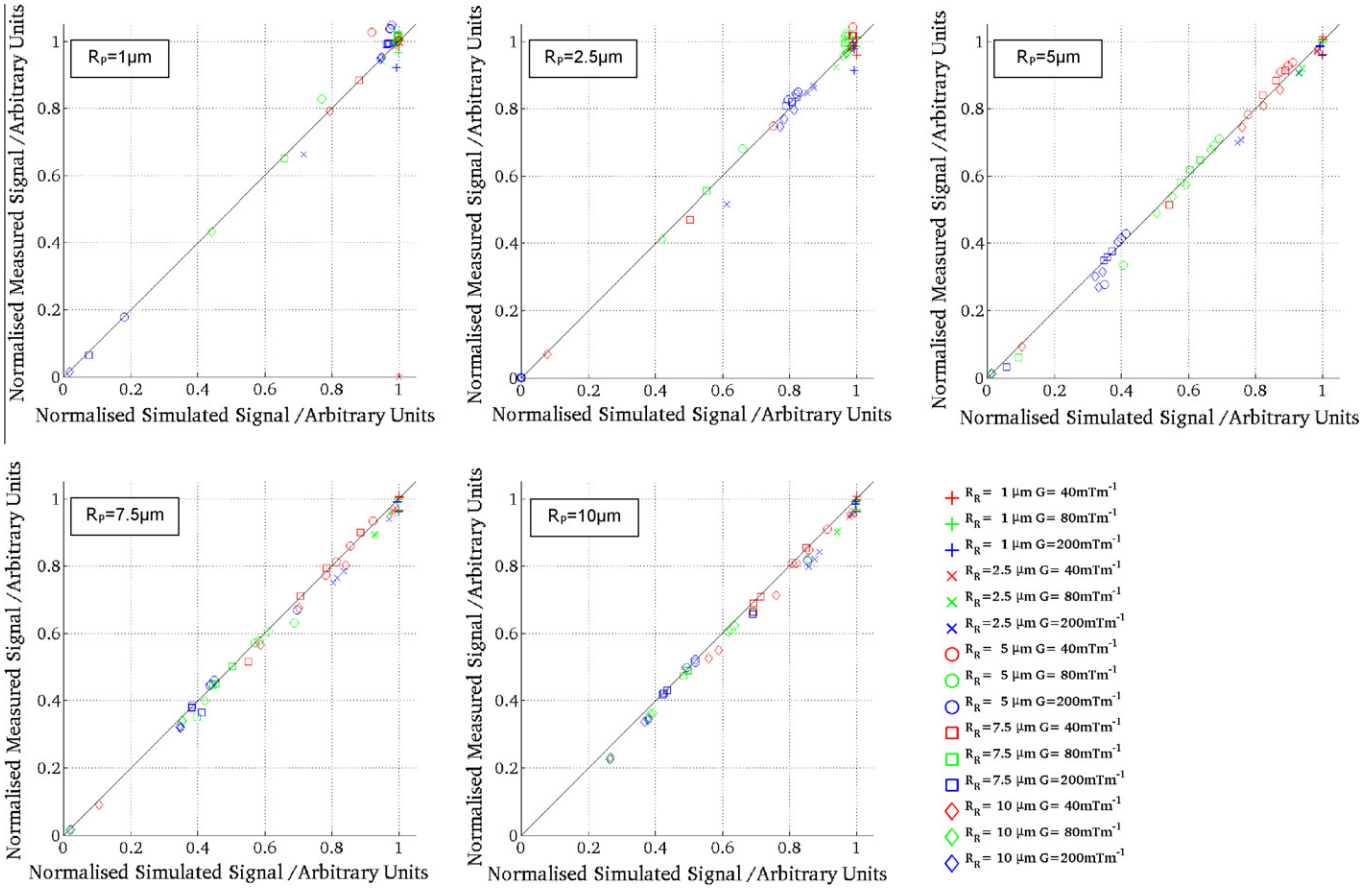

Fig. 4. Scatter plots of normalised mean measured signal against normalised simulated signal for each individual protocol, R_P. R_R is the radius of the microcapillary phantoms, G is the amplitude of the protocol containing the waveform. Axon radius index values, α_r, calculated from SEM measurements, are used in the tissue model to simulated signal. Each combination of colour and marker represents data from the four measurements in one protocol on one phantom at one gradient amplitude.

GEN and PGSE protocols are comparable. In addition, the distributions in Fig. 6 are narrower at 80 and 200 mT m^{-1} for both GEN and PGSE. The narrower distributions indicate that the radius estimates are more precise for GEN protocols and for higher maximum gradient amplitudes. Except for 1 μm pore radii, the modes of the histograms (Fig. 6) and the means (Table 3) are similar for both PGSE and GEN protocols.

Fig. 7 shows posterior distribution histograms for GEN protocols optimised for particular radii run on all the phantoms. The radius estimates are robust for all protocols, even for those that are optimised for different radii ($R_P \neq R_R$). By visual inspection of all the histograms in Fig. 7, we see that the mode of these distributions tend to be consistent with α_r, except for $R_R = 1$ μm. This is reflected in the means in Table 3, suggesting accurate radius estimates for both $R_P = R_R$ and $R_P \neq R_R$. In Fig. 7, the posterior distributions for specific R_R tend to be narrower (reflected in the smaller SD in Table 3) for $R_P = R_R$ compared to $R_P \neq R_R$ protocols. For example, $R_R = 5$ μm at gradient amplitude of 80 mT m^{-1}, the narrowest distribution (cyan in Fig. 7) and SD (comparing the s.d. in the bold and normal rows for $R_R = 5$ in Table 3) are when $R_P = 5$ μm. A notable exception to these observations is the estimate for $R_R = 5$ μm, $R_P = 1$ μm, $G = 40$ mT m^{-1}, which has a wide distribution and correspondingly high s.d., as well as being inconsistent with α_r.

For low R_R, the posterior distributions tend to be narrower as R_P decreases. Correspondingly, for high R_R, the posterior distributions tend to be narrower as R_P increases. These relationships are more marked for high R_R. Additionally, the mode (Fig. 7) and mean (Table 3) of posterior distributions for protocols optimised for large radii ($R_P = 7.5$ and 10 μm) tend to be more consistent with α_r.

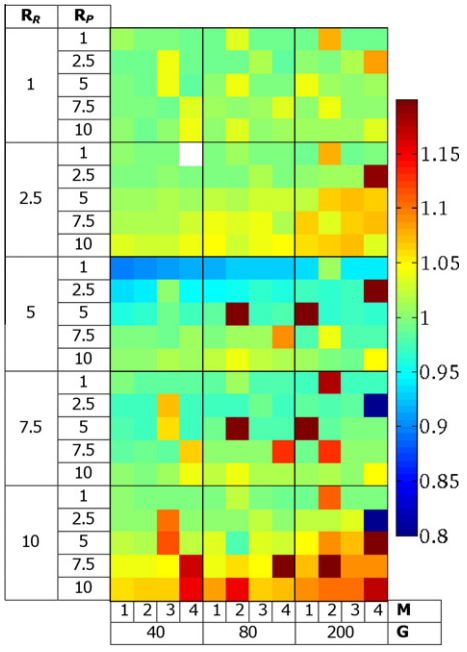

Fig. 5. Ratio of normalised simulated signal to normalised mean measured signal, for all combinations of phantom pore radius and GEN protocols. Green indicates agreement between measured and simulated signals; red indicates overestimation; blue indicates underestimation. R_R – Phantom pore radius (μm) R_P – Radius for which protocol is optimised for (μm) G – Maximum gradient strength (mT m^{-1}). M – Measurement number The $R_R = 2.5$, $R_P = 1$, $M = 4$ measurement is excluded due to incomplete execution of pulse sequence (white).

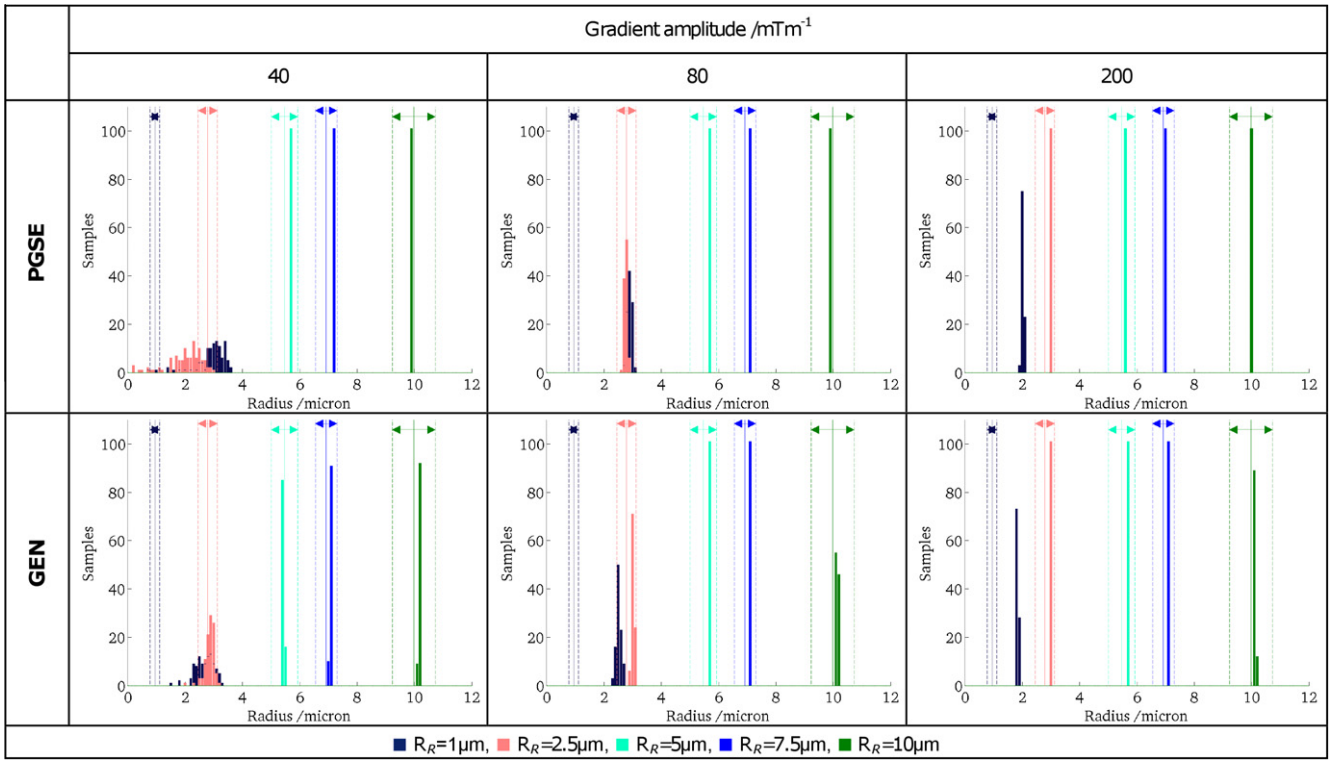

Fig. 6. Histograms of samples from the posterior distribution on the radius in which the protocol used corresponds to the radius of the pores in the phantom ($R_P = R_R$). For each particular histogram, distributions for phantoms with pore size 1, 2.5, 5, 7.5, 10 μm (coloured dark blue, pink, cyan, light blue, green, respectively) are shown. Gradient amplitudes of 40, 80, 200 mT m^{-1}are compared (columns) for optimised PGSE and GEN protocols (rows). Solid lines are the axon radius index, α_r, of the pores calculated from SEM measurements, and the dotted lines are the standard deviations as measured by SEM.

4. Discussion

Our results strongly suggest that the GEN waveforms can be implemented in practice on a small bore MRI scanner. We have shown good agreement between simulated and measured signal for protocols that are optimised for pore radii ranging from 1 to 10 μm, as in Fig. 4.

Furthermore, the standard deviation of the posterior distribution on the pore radius are smaller for GEN than for PGSE protocols, particularly at 40 mT m^{-1}. Our findings also suggest that accurate and precise pore estimates can be achieved for 2.5 μm radii at 40 mT m^{-1} gradient strength. This improved sensitivity compared to PGSE protocols at small pore radii is particularly significant when considering the distribution of axon radii in white matter tracts in the brain, where the majority of axon radii are under 5 μm [11], for example the modes of the axon radius distributions are around 1 μm and 0.5 μm in the rat optic nerve [23] and in the splenium of the human corpus callosum [41], respectively.

For GEN protocols, we find that the radius estimates are robust to the precise choice of protocol and gradient strength. For any particular R_R the posterior distribution is narrowest and least biased for the protocol for which $R_P = R_R$. However, for the most part, even $R_P \neq R_R$ protocols provide good estimates of R_R, which suggests we can find single protocols sensitive to a range of R_R. Although we optimise protocols for sensitivity to the nominal radius, we note that the range of radii to which a protocol is sensitive is likely to be much larger than the difference between R_P and α_r. Reoptimising for slightly perturbed radii produces little difference in the protocol.

GEN protocols for $R_P = 7.5$ and $R_P = 10$ μm tend to produce the most accurate and precise radius estimates across the whole range of R_R. Generally, it appears that these high R_P protocols retain sensitivity to low R_R better than low R_P protocols retain sensitivity to high R_R. For low R_P, the waveforms are highly specialised for sensitivity to low R_R and so lack sensitivity to high R_R. Overall this suggests we can get good sensitivity over the whole range of R_R studied here by focussing on $R_P \sim 7.5$ μm.

Posterior distributions are narrower for GEN than optimised PGSE protocols even though the duration of the GEN waveform is not fully optimised as it is for PGSE. In this study, water is used as the intra-capillary medium, which has a long T_2 (>600 ms), so the trade off between decreased signal to noise and T_2 attenuation is small: the attenuation due to T_2 is relatively small even at long TE used in this study. This is also reflected in the preliminary experiments using the GEN protocol, in which optimum echo times were evaluated by running trial optimisations at various echo times up to 127 ms (above this echo time, the signal was not consistent between repetitions): the objective function was lowest at the longest echo time permitted.

We note that, for GEN protocol, the optimisation algorithm may not find the global minimum of the objective function. However, suboptimality of the protocol should increase uncertainty rather than bias. Furthermore, optimisation of PGSE protocols is much simpler and we do find the global minimum reliably. Even so, we find that GEN protocols are more sensitive to small axon radii than PGSE protocols. The minimisation of the objective function is discussed further in [21,22,35].

A potential confounder is the presence of background magnetic field gradients due to the susceptibility difference between glass and water, which would introduce undesired cross-terms between the applied and background gradients, and also lower the T_2^* of the water. The 1 μm capillaries may be particularly affected by this since inner surface of these capillaries are relatively rough compared to the inner surface of capillaries that have greater pore size

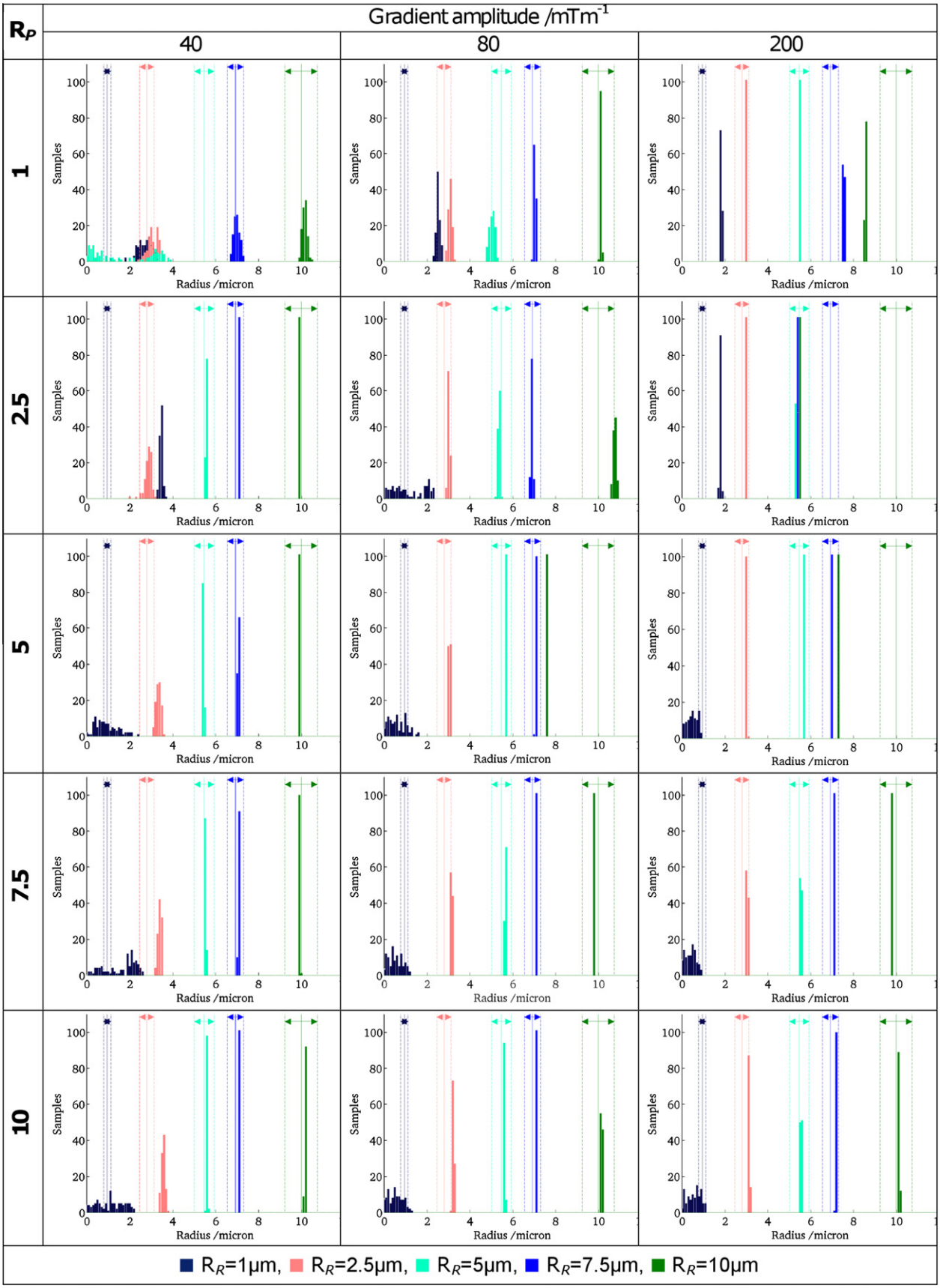

Fig. 7. Histograms of samples from the posterior distribution on the radius for all combinations of phantom pore radius, R_R, and GEN protocols, R_P. The colour scheme and lines follows Fig. 3. Rows contain histograms for GEN protocol optimised for one particular radius (top to bottom: protocol optimised for R_P = 1, 2.5, 5, 7.5, 10 μm). Columns contain histograms for various gradient amplitudes (left to right: 40, 80, 200 mT m^{-1}).

Table 3
The means and standard deviations of samples from the posterior distribution on the radius for all combinations of GEN protocols, R_P, and phantom pore radii, R_R, grouped by protocol, for 40, 80, 200 mT m^{-1} gradient amplitudes. Rows in bold show the data for when the protocol and the phantom pore radius correspond ($R_P = R_R$), for which data for optimised PGSE protocols are also shown.

R_P Radius for which protocol is optimised for/μm	R_R Phantom microcapillary radius/μm	GEN protocols Gradient amplitude (mT m^{-1})			PGSE protocols Gradient amplitude (mT m^{-1})		
		40	80	200	40	80	200
1	**1**	**2.6791 ± 0.3365**	**2.5192 ± 0.0878**	**1.8359 ± 0.0249**	**2.2393 ± 0.5748**	**2.8987 ± 0.0830**	**2.0237 ± 0.0358**
	2.5	3.0868 ± 0.2428	3.0787 ± 0.0772	2.9993 ± 0.0093			
	5	1.711 ± 1.4054	5.0393 ± 0.1223	5.5009 ± 0.0100			
	7.5	6.9801 ± 0.1418	7.0328 ± 0.0340	7.549 ± 0.0123			
	10	10.147 ± 0.1033	10.107 ± 0.0254	8.552 ± 0.0032			
2.5	1	3.4605 ± 0.0762	1.1818 ± 0.7561	1.803 ± 0.0312			
	2.5	**2.8557 ± 0.1686**	**3.0225 ± 0.0424**	**3.021 ± 0.0056**	**2.0416 ± 0.6188**	**2.7652 ± 0.0538**	**2.9896 ± 0.0103**
	5	5.5811 ± 0.0347	5.3632 ± 0.0459	5.3503 ± 0.0036			
	7.5	7.0806 ± 0.0089	6.8982 ± 0.0410	5.4119 ± 0.0023			
	10	9.8842 ± 0.0039	10.757 ± 0.0730	5.4651 ± 0.0019			
5	1	0.92135 ± 0.5255	0.62827 ± 0.4047	0.45513 ± 0.2542			
	2.5	3.3402 ± 0.1146	3.0497 ± 0.0206	3.0231 ± 0.0132			
	5	**5.419 ± 0.0262**	**5.7128 ± 0.0052**	**5.7154 ± 0.0039**	**5.7008 ± 0.0106**	**5.6829 ± 0.0046**	**5.5769 ± 0.0061**
	7.5	7.0544 ± 0.0119	7.0542 ± 0.0016	7.0204 ± 0.0011			
	10	9.9143 ± 0.0043	7.6105 ± 0.0009	7.2818 ± 0.0008			
7.5	1	1.6097 ± 0.7332	0.53491 ± 0.3230	0.39745 ± 0.2472			
	2.5	3.4013 ± 0.0797	3.1453 ± 0.0281	3.0488 ± 0.0127			
	5	5.5317 ± 0.0176	5.6555 ± 0.0103	5.5485 ± 0.0125			
	7.5	**7.0643 ± 0.0101**	**7.0965 ± 0.0061**	**7.1229 ± 0.0068**	**7.1806 ± 0.0062**	**7.1024 ± 0.0059**	**6.977 ± 0.0062**
	10	9.9387 ± 0.0041	9.8049 ± 0.0035	9.7932 ± 0.0024			
10	1	1.0898 ± 0.6235	0.5346 ± 0.3302	0.56792 ± 0.3058			
	2.5	3.5645 ± 0.0817	3.2337 ± 0.0367	3.1175 ± 0.0238			
	5	5.6077 ± 0.0220	5.627 ± 0.0164	5.5498 ± 0.0133			
	7.5	7.0814 ± 0.0146	7.0872 ± 0.0146	7.1792 ± 0.0145			
	10	**10.16 ± 0.0076**	**10.148 ± 0.0076**	**10.138 ± 0.0086**	**9.9092 ± 0.0069**	**9.9033 ± 0.0071**	**10.011 ± 0.0087**

Table 4
The relative standard deviation (s.d./mean) of the repetitions in the unweighted measurement before each acquisition set (δS0) and percentage difference between the means of unweighted measurements before and after each acquisition set (ΔS0).

R_R/μm	δS0/%	ΔS0/%
1	2.89	0.16
2.5	3.02	4.7
5	2.98	4.3
7.5	2.91	1.6
10	3.07	9.0

(personal communication, Noam Shemesh, Tel Aviv University, 2010). Indeed, we find that both T_2 and D_0 are smaller for $R_R = 1$ μm (Table 2). Attenuation due to these rough surfaces would tend to produce overestimates of radius, as is observed in our results. However, the presence of background gradients are likely to equally effect GEN and PGSE protocols as they have comparable weightings (Table 1). Biological samples are less likely to be affected by background gradients due to susceptibility differences, thus the estimates should not be shifted upwards.

Another potential confounder is associated with the system and sample stabilities. In particular, water leakage from the capillaries may effect the stability of the sample, however, we minimise potential effects by ensuring that the sensitive length of the r.f. coil is shorter than the length of the fibres. Intra-measurement variation is quantified by the relative standard deviation of the unweighted measurement taken before each acquisition set (δS0). Inter-measurement variation is quantified by the difference in the mean signal before and after each acquisition set (ΔS0). δS0 and ΔS0 values for the various radii are found in Table 4. There is no clear relationship between R_R and δS0, nor R_R and ΔS0, indicating that these variations are due to system rather than sample instabilities. Furthermore, we find that the mean signal of the unweighted measurement taken after each acquisition set falls within two standard deviations of the signal taken before the acquisition set for all R_R except for $R_R = 10$ μm (see Table 4). Indeed, in the case $R_P \neq R_R$, we do see that estimates for $R_R = 10$ μm are somewhat less robust than for other R_R. Nevertheless, estimates $R_R = 10$ μm and $R_P = R_R$ are robust. Also of note is the large drift between the measurements for $R_R = 5$ μm, $R_P = 1$ μm, $G = 40$ mT m^{-1} may account for the poor estimate.

In this study we have explored the radius estimates for various combinations of GEN protocols and pore diameters, finding that the estimate is most accurate for the a priori diameters used in the optimisation. In practice, a single GEN protocol, optimised for a range of diameters as in [22], would be used to map axon diameter index, providing a diameter estimate for each voxel. Furthermore, the optimisation extends naturally to arbitrary axon orientation [21,22].

This study shows that GEN protocols can be implemented on small bore scanners and that GEN protocols are more sensitive to small pore radius compared to equivalent PGSE protocols, especially at 40 mT m^{-1}. We plan to build on this work by optimising the GEN protocol for phantoms that contain multiple radii. This will inform us as to the most appropriate strategy for estimation of microstructural parameters in ex-vivo biological tissue. Future work will also compare optimised double wave-vector protocols [34,31–33] and protocols with oscillating waveforms [35–40]. In turn, this will provide valuable information for in vivo studies. The improved sensitivity to small pore sizes is likely to have significant benefits in disease models and in scenarios in which axon radius is a biomarker for disease progression or classification. Our findings suggest that the improved sensitivity to small axon radii of the GEN protocol would be reflected in clinical scenarios.

References

[1] P.T. Callaghan, A. Coy, T.P.J. Halpin, D. MacGowan, K.J. Packer, F.O. Zelaya, Diffusion in porous systems and the influence of pore morphology in pulsed gradient spin-echo nuclear magnetic resonance studies, J. Chem. Phys. 97 (1) (1992) 651–662, doi:10.1063/1.463979. <http://link.aip.org/link/?JCP/97/651/1>.

[2] A. Coy, P.T. Callaghan, Pulsed gradient spin-echo NMR 'diffusive diffraction' experiments on water surrounding close-packed polymer spheres, J. Colloid Interface Sci. 168 (2) (1994) 373–379, doi:10.1006/jcis.1994.1432. <http://www.sciencedirect.com/science/article/B6WHR-45P0SKG-F/2/27527cae563352e9bafc5360f3e6b913>.

[3] P.T. Callaghan, K.W. Jolley, J. Lelievre, Diffusion of water in the endosperm tissue of wheat grains as studied by pulsed field gradient nuclear magnetic resonance, Biophys. J. 28 (1) (1979) 133–141. <http://www.ncbi.nlm.nih.gov/pubmed/262443>.

[4] S. Godefroy, P.T. Callaghan, 2d relaxation/diffusion correlations in porous media, Magn. Reson. Imag. 21 (3–4) (2003) 381–383. <http://www.ncbi.nlm.nih.gov/pubmed/12850739>.

[5] N.L. Zakhartchenko, V.D. Skirda, R.R. Valiullin, Self-diffusion of water and oil in peanuts investigated by PFG NMR, Magn. Reson. Imag. 16 (5–6) (1998) 583–586. <http://www.ncbi.nlm.nih.gov/pubmed/9803914>.

[6] S. Umbach, E. Davis, J. Gordon, P. Callaghan, Water self-diffusion coefficients and dielectric properties determined for starch-gluten-water mixtures heated by microwave and by conventional methods, Cereal Chem. 69 (6) (1992) 637–642.

[7] Y.-Q. Song, S. Ryu, P.N. Sen, Determining multiple length scales in rocks, Nature 406 (6792) (2000) 178–181. <http://dx.doi.org/10.1038/35018057>.

[8] P.J. Basser, C. Pierpaoli, Microstructural and physiological features of tissues elucidated by quantitative-diffusion-tensor MRI, J. Magn. Reson. Ser. B 111 (3) (1996) 209–219. PMID: 8661285. <http://www.ncbi.nlm.nih.gov/pubmed/8661285>.

[9] D.L. Bihan, J. Mangin, C. Poupon, C.A. Clark, S. Pappata, N. Molko, H. Chabriat, Diffusion tensor imaging: concepts and applications, J. Magn. Reson. Imag. 13 (4) (2001) 534–546, doi:10.1002/jmri.1076. <http://doi.wiley.com/10.1002/jmri.1076>.

[10] C. Beaulieu, The basis of anisotropic water diffusion in the nervous system – a technical review, NMR Biomed. 15 (7–8) (2002) 435–455, doi:10.1002/nbm.782. <http://doi.wiley.com/10.1002/nbm.782>.

[11] S. Waxman, The Axon: Structure, Function, and Pathophysiology, Oxford University Press, New York, 1995.

[12] J.M. Ritchie, On the relation between fibre diameter and conduction velocity in myelinated nerve fibres, Proc. R. Soc. B: Biol. Sci. 217 (1206) (1982) 29–35, doi:10.1098/rspb.1982.0092. <http://rspb.royalsocietypublishing.org/cgi/doi/10.1098/rspb.1982.0092>.

[13] J. Piven, J. Bailey, B.J. Ranson, S. Arndt, An MRI study of the corpus callosum in autism, Am. J. Psych. 154 (8) (1997) 1051–1056.

[14] S. Cluskey, D.B. Ramsden, Mechanisms of neurodegeneration in amyotrophic lateral sclerosis, Mole. Pathol.: MP 54 (6) (2001) 386–392. PMID: 11724913. <http://www.ncbi.nlm.nih.gov/pubmed/11724913>.

[15] T. Heads, M. Pollock, A. Robertson, W.H. Sutherland, S. Allpress, Sensory nerve pathology in amyotrophic lateral sclerosis, Acta Neuropathol. 82 (4) (1991) 316–320. PMID: 1662002. <http://www.ncbi.nlm.nih.gov/pubmed/1662002>.

[16] P.L. Randall, Schizophrenia, abnormal connection, and brain evolution, Med. Hypoth. 10 (3) (1983) 247–280. PMID: 6877113. <http://www.ncbi.nlm.nih.gov/pubmed/6877113>.

[17] P.J. Basser, Inferring microstructural features and the physiological state of tissues from diffusion-weighted images, NMR Biomed. 8 (7) (1995) 333–344, doi:10.1002/nbm.1940080707. http://doi.wiley.com/10.1002/nbm.1940080707.

[18] G.J. Stanisz, G.A. Wright, R.M. Henkelman, A. Szafer, An analytical model of restricted diffusion in bovine optic nerve, Magn. Reson. Med. 37 (1) (1997) 103–111, doi:10.1002/mrm.1910370115. http://doi.wiley.com/10.1002/mrm.1910370115.

[19] Y. Assaf, R.Z. Freidlin, G.K. Rohde, P.J. Basser, New modeling and experimental framework to characterize hindered and restricted water diffusion in brain white matter, Magn. Reson. Med.: Off. J. Soc. Magn. Reson. Med./Soc. Magn. Reson. Med. 52 (5) (2004) 965–978, doi:10.1002/mrm.20274. PMID: 15508168. <http://www.ncbi.nlm.nih.gov/pubmed/15508168>.

[20] Y. Assaf, P.J. Basser, Composite hindered and restricted model of diffusion (CHARMED) MR imaging of the human brain, NeuroImage 27 (1) (2005) 48–58, doi:10.1016/j.neuroimage.2005.03.042. PMID: 15979342. <http://www.ncbi.nlm.nih.gov/pubmed/15979342>.

[21] D.C. Alexander, A general framework for experiment design in diffusion MRI and its application in measuring direct tissue-microstructure features, Magn. Reson. Med. 60 (2) (2008) 439–448, doi:10.1002/mrm.21646. <http://doi.wiley.com/10.1002/mrm.21646>.

[22] D.C. Alexander, P.L. Hubbard, M.G. Hall, E.A. Moore, M. Ptito, G.J. Parker, T.B. Dyrby, Orienta tionally invariant indices of axon diameter and density from diffusion MRI, NeuroImage 52 (4) (2010) 1374–1389, doi:10.1016/j.neuroimage.2010.05.043. <http://linkinghub.elsevier.com/retrieve/pii/S1053811910007755>.

[23] Y. Assaf, T. Blumenfeld-Katzir, Y. Yovel, P.J. Basser, AxCaliber: a method for measuring axon diameter distribution from diffusion MRI, Magn. Reson. Med.: Off. J. Soc. Magn. Reson. Med./Soc. Magn. Reson. Med. 59 (6) (2008) 1347–1354, doi:10.1002/mrm.21577. PMID: 18506799. <http://www.ncbi.nlm.nih.gov/pubmed/18506799>.

[24] D. Barazany, P.J. Basser, Y. Assaf, In vivo measurement of axon diameter distribution in the corpus callosum of rat brain, Brain: A J. Neurol. 132 (Pt 5) (2009) 1210–1220, doi:10.1093/brain/awp042. PMID: 19403788. <http://www.ncbi.nlm.nih.gov/pubmed/19403788>.

[25] H.H. Ong, A.C. Wright, S.L. Wehrli, A. Souza, E.D. Schwartz, S.N. Hwang, F.W. Wehrli, Indirect measurement of regional axon diameter in excised mouse spinal cord with q-space imaging: simulation and experimental studies, Neuroimage 40 (4) (2008) 1619–1632, doi:10.1016/j.neuroimage.2008.01.017. <http://dx.doi.org/10.1016/j.neuroimage.2008.01.017>.

[26] L. Avram, Y. Assaf, Y. Cohen, The effect of rotational angle and experimental parameters on the diffraction patterns and micro-structural information obtained from q-space diffusion NMR: implication for diffusion in white matter fibers, J. Magn. Reson. 169 (1) (2004) 30–38, doi:10.1016/j.jmr.2004.03.020. <http://www.sciencedirect.com/science/article/B6WJX-4C836V2-2/2/12e991c0a8f6d2fcf05264bd6a29a9a3>.

[27] L. Avram, E. Ozarslan, Y. Assaf, A. Bar-Shir, Y. Cohen, P.J. Basser, Three-dimensional water diffusion in impermeable cylindrical tubes: theory versus experiments, NMR Biomed. 21 (8) (2008) 888–898, doi:10.1002/nbm.1277. <http://dx.doi.org/10.1002/nbm.1277>.

[28] A. Bar-Shir, L. Avram, E. Ozarslan, P.J. Basser, Y. Cohen, The effect of the diffusion time and pulse gradient duration ratio on the diffraction pattern and the structural information estimated from q-space diffusion mr: experiments and simulations, J. Magn. Reson. 194 (2) (2008) 230–236, doi:10.1016/j.jmr.2008.07.009. <http://dx.doi.org/10.1016/j.jmr.2008.07.009>.

[29] D.G. Cory, A.N. Garroway, Measurement of translational displacement probabilities by NMR: an indicator of compartmentation, Magn. Reson. Med. 14 (3) (1990) 435–444.

[30] P.T. Callaghan, A. Coy, D. MacGowan, K.J. Packer, F.O. Zelaya, Diffraction-like effects in NMR diffusion studies of fluids in porous solids, Nature 351 (6326) (1991) 467–469. <http://dx.doi.org/10.1038/351467a0>.

[31] M.A. Koch, J. Finsterbusch, Compartment size estimation with double wave vector diffusion-weighted imaging, Magn. Reson. Med. 60 (1) (2008) 90–101, doi:10.1002/mrm.21514. <http://dx.doi.org/10.1002/mrm.21514>.

[32] N. Shemesh, E. Ozarslan, A. Bar-Shir, P.J. Basser, Y. Cohen, Observation of restricted diffusion in the presence of a free diffusion compartment: single- and double-pfg experiments, J. Magn. Reson. 200 (2) (2009) 214–225, doi:10.1016/j.jmr.2009.07.005. <http://dx.doi.org/10.1016/j.jmr.2009.07.005>.

[33] N. Shemesh, E. Ozarslan, P.J. Basser, Y. Cohen, Detecting diffusion–diffraction patterns in size distribution phantoms using double-pulsed field gradient NMR: theory and experiments, J. Chem. Phys. 132 (3) (2010) 034703, doi:10.1063/1.3285299. <http://dx.doi.org/10.1063/1.3285299>.

[34] P.P. Mitra, Multiple wave-vector extensions of the NMR pulsed-field-gradient spin-echo diffusion measurement, Phys. Rev. B Condens. Matter 51 (21) (1995) 15074–15078.

[35] I. Drobnjak, B. Siow, D.C. Alexander, Optimizing gradient waveforms for microstructure sensitivity in diffusion-weighted MR, J. Magn. Reson. 206 (1) (2010) 41–51, doi:10.1016/j.jmr.2010.05.017. PMID: 20580294, San Diego, Calif.: 1997. <http://www.ncbi.nlm.nih.gov/pubmed/20580294>.

[36] J. Stepisnik, Analysis of NMR self-diffusion measurements by a density matrix calculation, Physica B+C 104 (3) (1981) 350–364, doi:10.1016/0378-436(81)90182-0. <http://linkinghub.elsevier.com/retrieve/pii/0378436381901820>.

[37] P. Callaghan, A simple matrix formalism for spin echo analysis of restricted diffusion under generalized gradient waveforms, J. Magn. Reson. 129 (1) (1997) 74–84, doi:10.1006/jmre.1997.1233. <http://linkinghub.elsevier.com/retrieve/pii/S1090780797912337>.

[38] E.C. Parsons, M.D. Does, J.C. Gore, Temporal diffusion spectroscopy: theory and implementation in restricted systems using oscillating gradients, Magn. Reson. Med. 55 (1) (2006) 75–84, doi:10.1002/mrm.20732. <http://doi.wiley.com/10.1002/mrm.20732>.

[39] A.J.M. Kiruluta, Probing restrictive diffusion dynamics at short time scales, J. Magn. Reson. 192 (1) (2008) 27–36, doi:10.1016/j.jmr.2008.01.013. PMID: 18316215, San Diego, Calif.: 1997. <http://www.ncbi.nlm.nih.gov/pubmed/18316215>.

[40] J. Xu, M.D. Does, J.C. Gore, Sensitivity of MR diffusion measurements to variations in intracellular structure: effects of nuclear size, Magn. Reson. Med. 61 (4) (2009) 828–833, doi:10.1002/mrm.21793. <http://doi.wiley.com/10.1002/mrm.21793>.

[41] F. Aboitiz, A.B. Scheibel, R.S. Fisher, E. Zaidel, Fiber composition of the human corpus callosum, Brain Res. 598 (1–2) (1992) 143–153. <http://www.ncbi.nlm.nih.gov/pubmed/1486477>.

[42] M. Holz, S.R. Heil, A. Sacco, Temperature-dependent self-diffusion coefficients of water and six selected molecular liquids for calibration in accurate 1H NMR PFG measurements, Phys. Chem. Chem. Phys. 2 (20) (2000) 4740–4742, doi:10.1039/b005319h. <http://xlink.rsc.org/?DOI=b005319h>.

[43] I. Drobnjak, H. Zhang, M.G. Hall, D.C. Alexander, The matrix formalism for generalised gradients with time-varying orientation in diffusion NMR, J. Magn. Reson. Corrected Proof, in press, doi:doi:10.1016/j.jmr.2011.02.022. <http://www.sciencedirect.com/science/article/B6WJX-529MVPV-1/2/271b3b2da834219248e6502e1e5c2f37>.